Supplementary control based on current source coupling for improving dynamic characteristics of active distribution network

Hou, Jue ; Liu, Zhou ; Wang, Shaorong ; Chen, Zhe; Xie, Wei; Fang, Cheng; Wei, Xinchi ; Popov, Marjan

DOI
10.1016/j.ijepes.2021.107525

Publication date
2022

Document Version
Final published version

Published in
International Journal of Electrical Power and Energy Systems

Electrical Power and Energy Systems 135 (2022) 107525

Contents lists available at ScienceDirect

International Journal of Electrical Power and Energy Systems

journal homepage: www.elsevier.com/locate/ijepes

Supplementary control based on current source coupling for improving dynamic characteristics of active distribution network

Jue Hou [a], Zhou Liu [b,*], Shaorong Wang [a], Zhe Chen [b], Wei Xie [c], Chen Fang [c], Xinchi Wei [c], Marjan Popov [d]

[a] State Key Laboratory of Advanced Electromagnetic Engineering and Technology, School of Electrical and Electronic Engineering, Huazhong University of Science and Technology, Wuhan 430074, China
[b] Department of Energy and Technology, Aalborg University, DK-9220 Aalborg, Denmark
[c] The State Grid Shanghai Municipal Electric Power Company, Shanghai 200122, China
[d] Delft University of Technology, Faculty of EEMCS, Delft, the Netherlands

ARTICLE INFO

Keywords:
Supplementary control
Active distribution network
Converter controller
Eigenvalue analysis
Hardware in the loop
RTDS

ABSTRACT

Supplementary control (SC) technology is widely leveraged by power supply companies in active distribution networks (ADNs) to improve their stability and dynamic characteristics. Yet, the existed SCs are generally implemented from inside the converter controllers of distributed generators (DGs) or active loads, so there is a need to redesign the internal physical structure of the existing controller, resulting in the increasing work amount of assembling and workability. This paper studies the specific R & D process of a novel external coupling type SC (ECSC), which is based upon current source injection (CSI-ECSC) for improving the dynamic characteristics of ADN. The SC current signals are coupled to the current sampling loop from outside the converter controller. And the employment of the existing current sample makes it unnecessary to redesign the internal physical structure of the existing controller. As a result, the SC assembling is simplified and its workability is improved. In this paper, a detailed exemplary ADN with direct-drive permanent magnet synchronous generator (PMSG) is firstly set up in math for full eigenvalue analysis. Then, the CSI-ECSC is designed with its control loop, interface circuit, and parameter setting. Furthermore, by using PSCAD/EMTDC, groups of case studies are conducted in ADNs where photovoltaics (PVs) and energy storage (ES) are included. Finally, the real-time hardware-in-the-loop (HIL) testing validates the functionality of the realized CSI-ECSC in RTDS.

1. Introduction

The integration of distributed energy resources (DERs) and active loads in active distribution networks (ADNs) through power electronic converters such as wind generations (WGs), solar photovoltaics (PVs), and electric vehicles (EVs) is growing fast now, and this growth is predicted to be an even greater rate in the future [1–4]. However, due to intermittent characteristics and uncertain events (such as contingencies and system faults) in either power source side or load side of converter-based units, the system instabilities under some emergency operating conditions would occur [5–7]. Furthermore, with the increasing applications of multiple electronic converters integrated in some small-scaled ADNs, the interaction and coupling effect might result in local power oscillation [8–10].

Nowadays, supplementary control (SC) is regarded as one solution for improving the dynamic characteristics of power system [11–13]. For instance, power system stabilizers (PSSs) are employed to suppress low frequency oscillation in power systems [14,15]. Static var compensators (SVCs) and static synchronous compensators (STATCOMs) are used in power systems to enhance their stability [16,17]. While in ADNs, most of SC methods are based on converter controllers. And the existing working steps of SC strategy can be summarized as follows: (1) Sample the selected disturbance signals such as power and voltage; (2) Produce supplementary signals by adjusting the phase and magnitude of disturbance signals; (3) Feedback the supplementary signals through the converter control loop to form an additional channel to improve the dynamics [18–21].

In line with the above three steps, scholars have undertaken

* Corresponding author.
E-mail addresses: houjue@hust.edu.cn (J. Hou), zli@et.aau.dk (Z. Liu), wsrwy96@vip.sina.com (S. Wang), zch@et.aau.dk (Z. Chen), xiew@sh.sgcc.com.cn (W. Xie), fangc02@139.com (C. Fang), newlate@126.com (X. Wei), M.Popov@tudelft.nl (M. Popov).

https://doi.org/10.1016/j.ijepes.2021.107525
Received 25 December 2020; Received in revised form 23 July 2021; Accepted 15 August 2021
Available online 3 September 2021

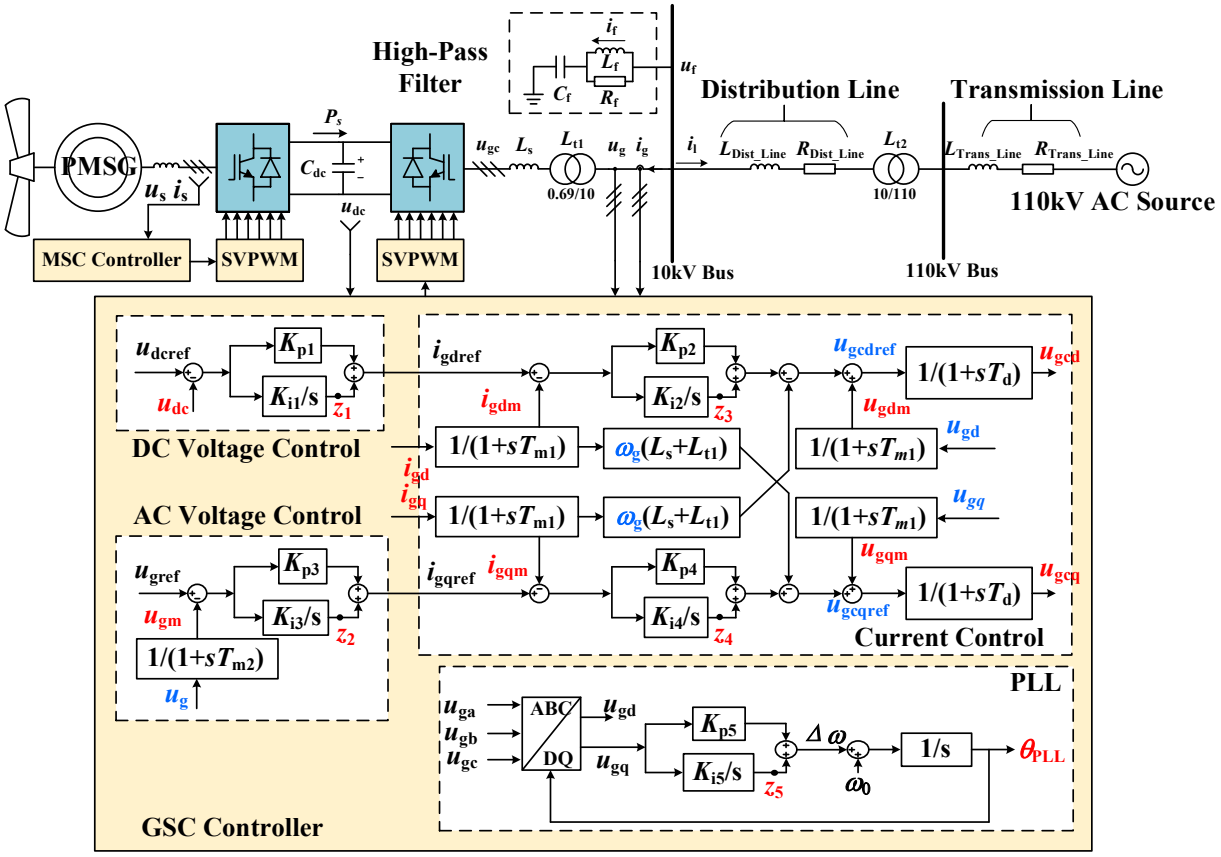

Fig. 1. Connection structure diagram and control system of the target system.

extensive research into SC and have proposed numerous SC schemes to enhance the system stability in ADNs. Most of the existing SC is implemented from inside the grid-side converter (GSC) controllers [22–25]. In [22], a supplementary angle droop control is proposed inside each DG converter to stabilize the system for a range of operation conditions while ensuring satisfactory load sharing. And a gain-scheduled decoupling strategy is presented to enhance the transient performance and stability of an islanded ADN through a supplementary control proposed in [23]. A novel additional control strategy for parallel DG inverters in ADN is presented in [24] to achieve good active and reactive power sharing. In [25], a traditional supplementary sub-synchronous damping control (SSDC) is presented for damping sub-synchronous oscillation among direct-drive permanent magnetic synchronous generators (PMSGs).

Despite the above methods produced favorable performances, it is still complicated by superposing SC signals upon reference signals inside the controllers. Furthermore, once the all-in-one packaging of controllers has been finished and assembled to the main circuit of the converter, it may not be feasible to have any new SC assembling. But, if we design a totally new converter controller to replace the existing one for extra SC functions, the frequent re-construction work of the converter controllers would result in low efficiency, and high-cost assembling and management.

These facts motivate us to develop an external SC to fulfill the requirements of modular design and implementation, which is independent from the existing converter controller. In this paper, we propose a novel current source injection based-external coupling type SC (CSI-ECSC) to improve the performance of converter-based DGs' controllers.

The main contributions of this paper are as follows:

1) It is an attempt to develop an external SC based on current injection. The implementation mode of injecting AC current signals into current sampling loop of GSC controller has not been discussed before in the literature.
2) The entire CSI-ECSC is an independent modular design, which prevents redesigning the internal structure of the original controller.
3) The CSI-ECSC can be widely applied for diverse types of converter-based units. In other words, any DG or active load integrated to ADNs with electronic converter such as PMSG, PV, and ES, etc. can apply the CSI-ECSC, because it is made according to the specific existing control of converter controller.
4) This work is illustrated through comprehensive and detailed research and development process, including full eigenvalue analysis, interface circuit design, detailed simulation comparison, and effectiveness verification in hard-in-the-loop (HIL) testing based on real-time digital simulator (RTDS) system.

The rest of the paper is structured as follows. The state space mathematical model and the dynamic process of an exemplary ADN are introduced in Section 2. Section 3 conducts specific design of the CSI-ECSC. Then, Section 4 illustrates case studies in simulation in different ADNs with PMSG, PV, and EV. In Section 5, a real-time HIL testing procedure validates the functionality of the realized CSI-ECSC in RTDS. Finally, Section 6 concludes the paper.

2. State space mathematical model and dynamic process

In this section, the state space model of the ADN system is formulated, in which direct-drive permanent magnet synchronous generator (D-PMSG) is connected to power grid through distribution line. Based on the mathematical model, the eigenvalues of the system under different working conditions are calculated to analyze the system stability. And the system dynamic simulation is conducted to verify the correctness and feasibility of the developed models.

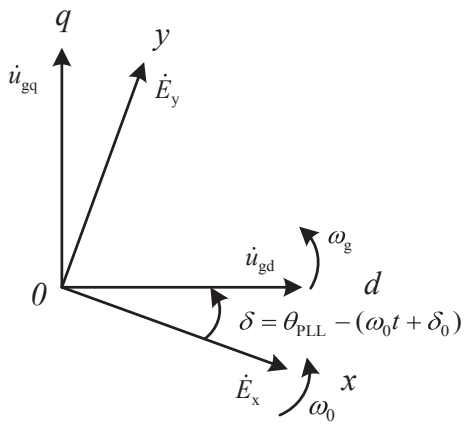

Fig. 2. Vector graph of coordinate transformation between the synchronous rotating coordinate system of GSC and that of infinite system.

2.1. State space model of target system based on small-signal method

In order to build up detailed model of one test system with PMSG, a small perturbation method is used for power system static stability research and judgment. The steps of setting up a small signal dynamic model are as follows: (1) Develop the nonlinear differential equations of system under DQ coordinate system, based on the selected state variables and algebraic variables. (2) Linearize the differential equation and algebraic equation respectively. (3) Eliminate the algebraic variables in the equation. (4) Formulate matrix $\boldsymbol{A}$ after the initial state calculation for given operation condition is conducted. (5) Define static stability of system under given conditions, based on the eigenvalue analysis of a matrix $\boldsymbol{A}$ [26–28].

The diagram of the example test system with D-PMSG connected to power grid through distribution line is shown in Fig. 1. Due to the decoupling control effect of the back-to-back converter, PMSG is mainly controlled by the machine-side converter (MSC) controller. The output power P_s of MSC is decided by the power generated b wind turbine (WT). Thus, this part could be simplified when the WT power is constant. At AC side, the GSC is connected to the low voltage side (0.69 kV) of the 0.69/10 transformer by inductance L_s. The high voltage side (10 kV) of the transformer is connected to a 10 kV bus, where an RLC high-pass filter (HPF) is installed [29,30]. This 10 kV bus is connected to the 110 kV bus through an overhead distribution line (OHL) and a 10/110 transformer. The grid is represented by a 110 kV infinite power source, which is connected to the 110 kV bus through an overhead transmission line. Both lines are modeled by equivalent RL circuit, where $L_{\text{Dist\_Line}}$ and $R_{\text{Dist\_line}}$, $L_{\text{Trans\_Line}}$ and $R_{\text{Trans\_line}}$ are defined to represent the distribution line and transmission line respectively. are The GSC controller samples three-phase current i_g at PCC and DC voltage u_{dc}, and outputs AC voltage reference u_{gref} to GSC. All related parameters and variables are listed in Tables A1 and A2.

The GSC controller is composed of AC voltage control, DC voltage control, and current loop. Also, a first-order lag is designed for representing measurement and sample link. In Fig. 1, the state variables are shown in red, and the algebraic variables are shown in blue. The state space mathematical model of the target system could be divided into the following parts, namely, AC system, DC capacitor, measurement and sample link, outer and inner loop control system, phase-locked loop (PLL), converter switching and modulation, and coordinate transformation [31–33]. State space equations of target system are shown in Appendix B.

Fig. 2 shows a vector graph of coordinate transformation between the DQ synchronous rotating coordinate system of GSC and the XY one of infinite grid system. The vector control based on grid voltage orientation is adopted in GSC, where the voltage phasor of PCC $\dot{u}_g$ is utilized as reference to acquire DQ coordinate system, and the rotation angle of its D-axis vector $\dot{u}_{gd}$ is θ_{PLL}. But the grid XY rotating coordinate system takes the voltage phasor of power system $\dot{E}$ as reference, and the rotation

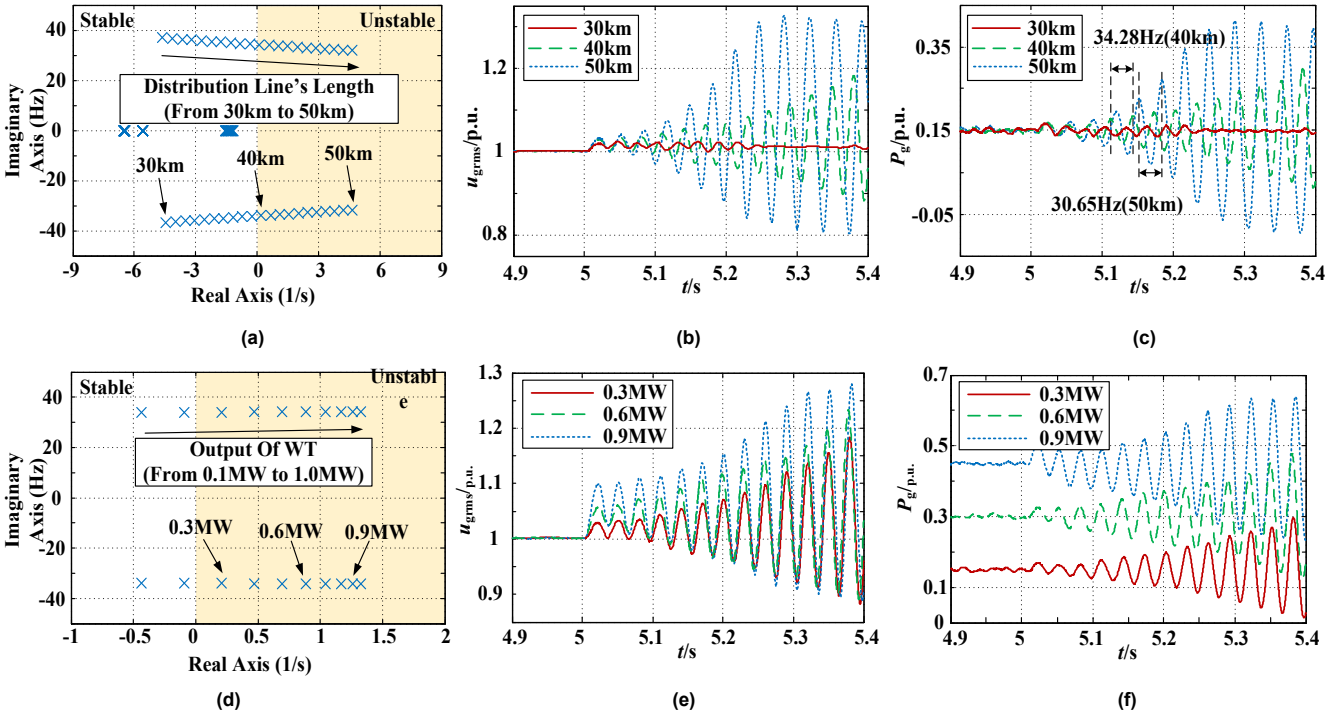

Fig. 3. Root loci in theory and waveforms in simulation (a) Root loci as length of distribution line changes, (b) Waveforms of effective value of AC voltage u_{grms} at PCC as length of distribution line changes, (c) Waveforms of effective value of active power P_g at PCC as length of distribution line changes, (d) Root loci as output power of WT changes, (e) Waveforms of effective value of AC voltage u_{grms} at PCC as output power of WT changes, (f) Waveforms of effective value of active power P_g at PCC as output power of WT changes.

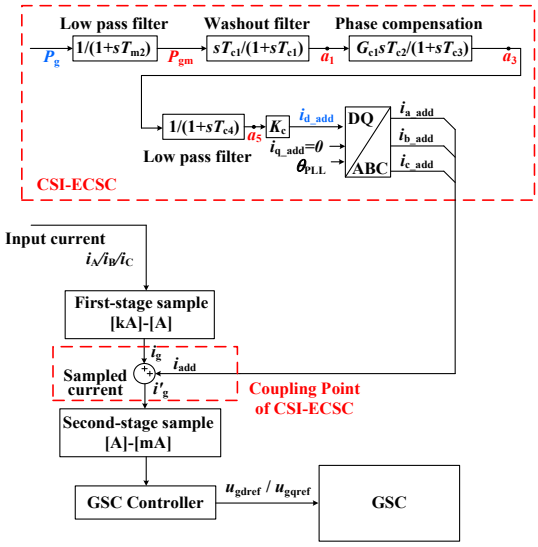

Fig. 4. CSI-ECSC scheme outside the GSC controller.

angular velocity and the initial phase angle of related X-axis vector $\dot{E}_x$ are ω_0 and δ_0 [34].

Based on the linearization of equations in Appendix B, a small signal dynamic model is established, as shown in Eq. (1). And 22-dimensional corresponding state variables $\Delta \boldsymbol{X}$ and 9-dimensional algebraic variables $\Delta \boldsymbol{Y}$ are shown in Eq. (2) and Eq. (3), respectively. In Eq. (4), after $\Delta \boldsymbol{Y}$ is eliminated, the system coefficient matrix $\boldsymbol{A}_{\mathbf{PMSG}}$ is calculated.

$$\begin{cases} \dfrac{\mathrm{d}\Delta \boldsymbol{X}}{\mathrm{d}t} = \boldsymbol{A}\Delta \boldsymbol{X} + \boldsymbol{B}\Delta \boldsymbol{Y} \\ \boldsymbol{0} = \boldsymbol{C}\Delta \boldsymbol{X} + \boldsymbol{D}\Delta \boldsymbol{Y} \end{cases} \tag{1}$$

$$\Delta X = \left[\Delta u_{dc}, \Delta i_{gd}, \Delta i_{gq}, \Delta i_{fd}, \Delta i_{fq}, \Delta u_{fd}, \Delta u_{fq}, \Delta i_{ld}, \Delta i_{lq}, \Delta i_{gdm}, \Delta i_{gqm}, \Delta u_{gdm}, \Delta u_{gqm}, \Delta z_1, \Delta z_2, \Delta z_3, \Delta z_4, \Delta z_5, \Delta \theta_{PLL}, \Delta u_{gm}, \Delta u_{gcd}, \Delta u_{gcq}\right]^T \tag{2}$$

$$\Delta Y = \left[\Delta u_{gd}, \Delta u_{gq}, \Delta \omega_g, \Delta u_g, \Delta E_x, \Delta E_y, \Delta \delta, \Delta u_{gcdref}, \Delta u_{gcqref}\right]^T \tag{3}$$

$$\begin{cases} \dfrac{\mathrm{d}\Delta X}{\mathrm{d}t} = A_{PMSG}\Delta X \\ A_{PMSG} = A - BD^{-1}C \end{cases} \tag{4}$$

2.2. Oscillation analysis in target system

In this part, based on the established small signal model, eigenvalue analysis is conducted to investigate dynamic characteristics of the exemplary target system. Time-domain simulation is used as a verification tool.

Since renewable energy sources are time-varying and stochastic on power output, the power fluctuations might take place in ADNs. Due to some sudden events, e.g., operation modes switching, fault occurrences, and other disturbances, the interaction effects between the GSCs' controllers in a small-scale area can provoke oscillations. Consequently, for D-PMSG, small disturbances like gust wind and sudden changes of distribution lines can cause the power flow oscillations and voltage violations.

Fig. 3 (a) shows parts of system root loci when the length of distribution line is changed from 30 km to 50 km. Theoretically speaking, while the distribution line becomes longer, the dominant poles move toward the right half plane. When the length of distribution line is larger than 40 km, the dominant poles move into the right half of plane. Corresponding to the oscillation frequency increase with the line length from 34.06 Hz under 40 km to 30.84 Hz under 50 km, the imaginary part of the dominant poles becomes smaller. Fig. 3 (b) and (c) show the waveforms of AC voltage u_{grms} and active power P_g at PCC respectively when the length of distribution line changes. When the length of distribution line is 30 km, both u_{grms} and P_g start to oscillate at 5.0 s and begin to stabilize after several oscillation periods, which means the system remains stable basically. But, when its length becomes longer, the oscillations of u_{grms} and P_g are quite severe and the longer the length is, the lower the oscillation frequencies are. The simulation verification matches well with above theoretical analysis. Fig. 3 (d) shows the parts of root loci when the output power of WT is changed from 0.1 MW to 1.0 MW. It can be seen that, with the increase of WT output power, the system stability turns worse. The oscillation frequency under the WT output power of 0.3 MW, 0.6 MW, and 0.9 MW, is 34.06 Hz, 34.13 Hz, and 34.2 Hz, respectively. As can be seen from the simulation results in Fig. 3 (e) and (f), the systems under all three conditions start to oscillate at 5.0 s. The higher the output power of WT is, the greater the amplitude of oscillation waveforms is, which means the system turns more unstable as the WT output power increases. And there are almost no changes in oscillation frequency under all the three conditions. Thus, the developed mathematical model describes the dynamic performance of target system quantitatively and precisely.

3. Control principle of CSI-ECSC

In this section, the introduction of current-source-injection-based external-coupling-type supplementary control will be focused. Combined with small signal model of the target system, a mathematical model of CSI-ECSC is set up for analyzing the control effect. Three key parameters are defined, based on the proposed determination method.

3.1. Structure of CSI-ECSC

This part introduces the specific control links and interface circuit of the proposed CSI-ECSC.

The CSI-ECSC is equipped in the current signal sampling loop at PCC of GSC. The coupling method of additional signal uses the current transformers to superimpose three-phase current additional signals to the original sampled current signals of GSC according to Kirchhoff's current law (KCL). This additional signal coupling method puts forward a new assembly method of supplementary controller, which ensures the independence of both GSC controller and supplementary controller. It would no longer be necessary to change the inner physical structure of GSC controller. The supplementary control signal is decided as the current signal rather than the voltage signal, since the change of the input voltage in the converter controller will lead to the malfunction of the related PLL normally.

As shown in Fig. 4, the proposed CSI-ECSC is attached to the current sampling loop of GSC controller. It is comprised of input low pass filter, washout filter, phase compensation, output low pass filter, gain link, and Inverse Park Transformation. It monitors the active power fluctuation which is calculated by voltage u_g and current i_g at PCC, and outputs the three-phase AC supplementary coupling current signal i_{add}. The low-pass filter is used to pick out the concerned signal and avoid interference on the normal control function of GSC. The design of washout filter and phase compensation is for filtering DC component and adjusting magnitude to improve phase stability margin. The output low pass filter is designed for simulating time delay and output current transformers. The gain link is designed to control the amplitude of supplementary signal. After that, D-axis component of supplementary current $i_{\mathrm{d\_add}}$ is calculated. By making Q-axis component of supplementary current $i_{\mathrm{q\_add}}$ zero, the three phases supplementary current signals ($i_{\mathrm{a\_add}}$, $i_{\mathrm{b\_add}}$, and $i_{\mathrm{c\_add}}$) are generated by Inverse Park Transformation, and then sent out between two current sampling stages of GSC controller.

In general, GSC controller adopts two-stage sampling, which could reduce voltage from kilovolts to volts and current from hundreds of amps to milliamps in GSC controller. Fig. 5 shows the hardware interface

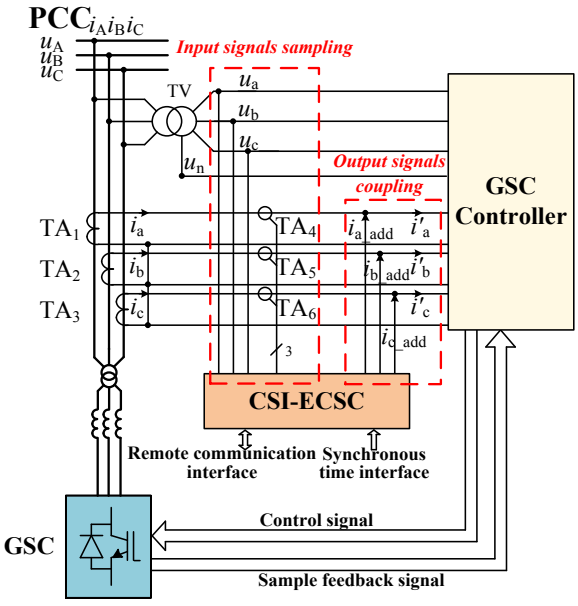

Fig. 5. Hardware interface circuit of CSI-ECSC.

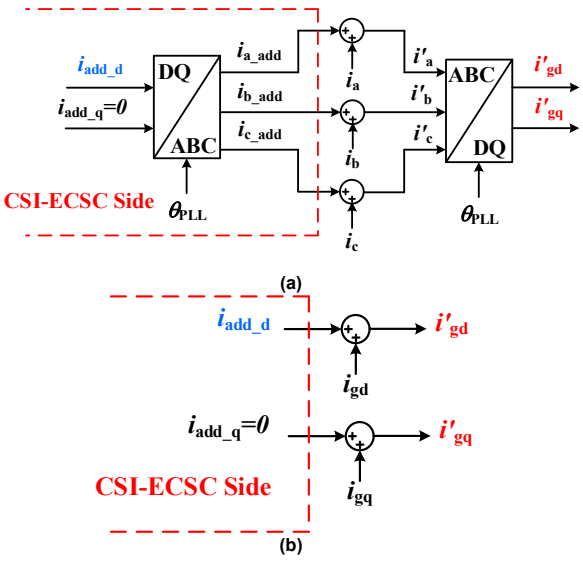

Fig. 6. Equivalent process of supplementary current signal coupling, (a) Actual block diagram of supplementary current signal coupling, (b) Equivalent block diagram of supplementary current signal coupling.

circuit of the developed CSI-ECSC, which contains the input signals sampling and the output signals coupling. TV, TA_1, TA_2, and TA_3 are the first-stage transformers (kilovolts to hundreds of volts and hundreds of amps to amps). And the second-stage transformers TA_4, TA_5, and TA_6 (hundreds of volts to volts and amps to milliamps) are encapsulated in GSC controllers. Signals coupling point of CSI-ECSC is in the middle of the two stages. According to KCL, three phases of input current signals i'_a, i'_b, and i'_c are decided by the three phases of supplementary current i_{a_add}, i_{b_add}, and i_{c_add} superimposed by the three phases of first-stage sampling current i_a, i_b, and i_c, respectively. By injecting relatively small current, the power demand of CSI-ECSC is very low. In this way, the proposed CSI-ECSC does not change inner physical structure of GSC controller, and its control effect is based on the response of the original controller.

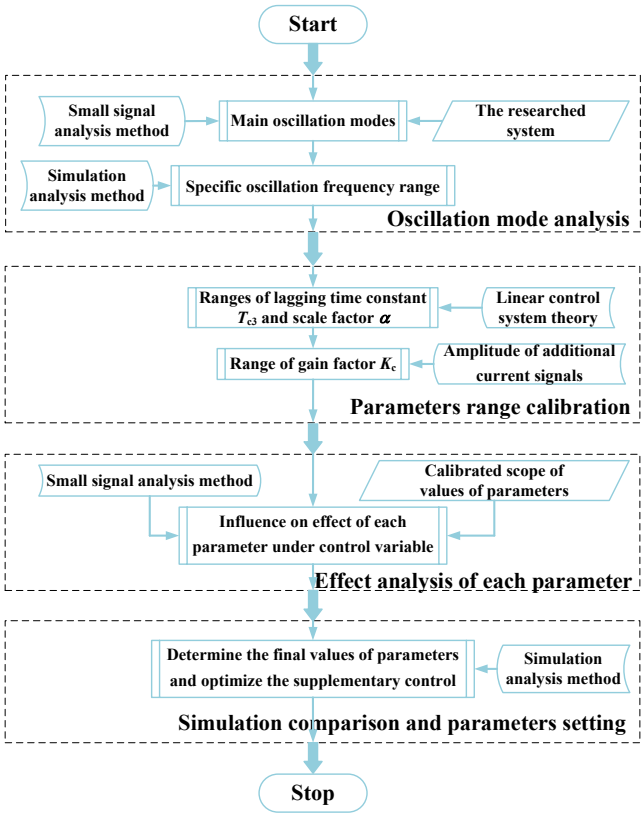

Fig. 7. Flow chart of parameter setting and optimization method.

3.2. Mathematical model of CSI-ECSC

After the introduction of specific links and interface circuit, this part will set up the small signal model of the proposed CSI-ECSC using an equivalent method to combine the external coupling with the inner control loop.

Since CSI-ECSC's supplementary current signals coupling process is at AC side, it is necessary to conduct Park transformation and related inverse transformation for the connection of small signal dynamic models under different coordinate systems. Fig. 6 shows the equivalent process of supplementary current signal coupling. The coupling of i_{add} and i_g is between a park transformation and a reverse park transformation as shown in Fig. 6 (a). Therefore, the whole coupling process can be transferred to DQ-side of park transformation equivalently as shown in Fig. 6 (b). In this way, a small signal dynamic model of the CSI-ECSC could be set up and added to the model of the system.

Similarly, the state variables (shown in red) and the algebraic variables (shown in blue) are chosen, as shown in Fig. 4 and Fig. 6. The nonlinear differential equations of

the system under three-phase coordinate system are deduced. After standardization and coordinate transformation, the state space equations under DQ coordinate system are put forward as shown from Eq. (5) to Eq. (11). Then, after the state space equations are linearized, the small signal dynamic model of system adopting CSI-ECSC is finally set up.

$$\frac{\mathrm{d}}{\mathrm{d}t}\begin{bmatrix} a_2 \\ a_4 \\ a_5 \end{bmatrix} = \begin{bmatrix} 1 & 0 & 0 \\ 0 & 1 & 0 \\ 0 & 1/T_{c4} & -1/T_{c4} \end{bmatrix} \begin{bmatrix} a_1 \\ a_3 \\ a_5 \end{bmatrix} \tag{5}$$

$$\frac{\mathrm{d}}{\mathrm{d}t}P_{gm} = \frac{1}{T_{m2}}P_g - \frac{1}{T_{m2}}P_{gm} \tag{6}$$

$$\frac{\mathrm{d}}{\mathrm{d}t}i_{gdm} = \frac{1}{T_{m1}}i'_{gd} - \frac{1}{T_{m1}}i_{gdm} + \frac{1}{T_{m1}}i_{d\_add} \tag{7}$$

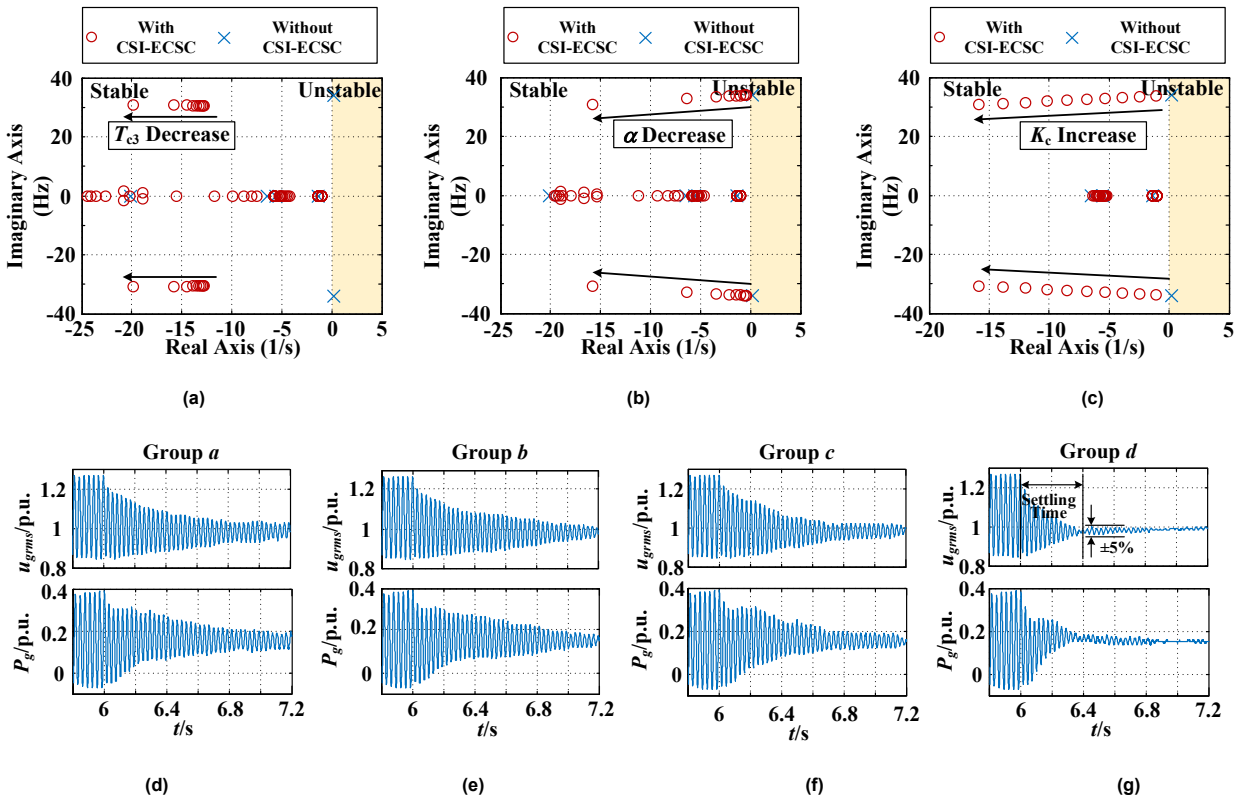

Fig. 8. Root loci and waveforms of u_{grms} and P_g at PCC of the system with CSI-ECSC under variation of key parameters, (a) Root loci under T_{c1} changes, (b) Root loci under α changes, (c) Root loci under K_c changes, (d) Waveforms of u_{grms} and P_g at PCC under variation of key parameters.

$$a_1 + \frac{1}{T_{c1}} a_2 - P_g = 0 \tag{8}$$

$$G_{c1} a_2 - a_4 + G_{c1} T_{c3} a_1 - T_{c2} a_3 = 0 \tag{9}$$

$$K_c a_5 - i_{d\_add} = 0 \tag{10}$$

$$P_g + u_{gd} i_{gd} + u_{gq} i_{gq} = 0 \tag{11}$$

3.3. Parameter setting and optimization method of CSI-ECSC

In order to improve the applicability of the proposed CSI-ECSC, a systematic parameter design process is introduced in this subsection.

The oscillation modes turn to be completely different under different working conditions. And as a reference for controller design under multiple conditions of different systems, the parameter setting and optimization method of the developed CSI-ECSC could be specified in flow chart as shown in Fig. 7:

1) **Oscillation mode analysis**: Use small signal analysis method to figure out the main oscillation mode of the target system. Clarify the specific oscillation frequency range of the system under this condition.
2) **Parameters range calibration**: In linear control system theory, based on the basic design method [18], the value range of lagging time constant T_{c3} and scale factor α can be determined. And the task of designing K_c involves the amplitude of additional current signals which are injected to current sampling loop of GSC controller.
3) **Effect analysis of each parameter**: In the calibrated scope of parameter values, small signal analysis method is used to study influence on supplementary control effect of each parameters under control variable.
4) **Simulation comparison and parameter setting**: Corresponding to the effect analysis, simulations will be conducted among several groups of parameter values. After that, the final value can be determined and the optimization of the developed supplementary control will be achieved.

4. Case study of CSI-ECSC

In this section, dynamic characteristic optimization effect of CSI-ECSC will be validated by simulation. Firstly, in the system of D-PMSG connected to power grid through distribution line, the study on parameter setting is conducted. Then, a comparison is made between traditional damping control and CSI-ECSC. Finally, CSI-ECSC is applied to an ADN with photovoltaics (PVs) and energy storage (ES) to verify its effect in different systems.

4.1. Performance study of the CSI-ECSC based on parameter setting

Adopting the parameter setting and optimization method, we conducted performance study of CSI-ECSC in this part. As analyzed above, by changing length of distribution line or output of WT, subsynchronous oscillation would take place in the target system with frequency of 30 ~ 35 Hz.

The task of designing the compensation link, whose design process is described in [18], involves the specification of lagging time constant T_{c3} and the scale factor α. Based on a phase compensation scope ranging from 0 to 54 degrees and an oscillation frequency scope from 20 Hz to 50 Hz, the scope of lagging time constant T_{c3} and scale factor α are determined as from 0.01 s to 0.1 s and from 2.0 to 10.0, respectively.

And the task of K_c tuning is related to the amplitude of additional current signals which are injected into the existing current sampling loop of the GSC controller. The amplitude of those signals is mainly influenced by the following two considerations. On the one hand, in

Table 1
Parameters of supplementary control for simulation verification.

Parameters	T_{c3}	α	K_c
Group a	0.1 s	10.0	0.7
Group b (only α changes)	0.1 s	2.0	0.7
Group c (only T_{c3} changes)	0.02 s	2.0	0.7
Group d (only K_c changes)	0.02 s	2.0	1.0

Table 2
Differences between CSI-ECSC and traditional SCs.

Contrastive SC works	Types of SC signals	SC signals coupling points	SC signals coupling types	SC assembly mode
[22]	Voltage	D-axis and Q-axis voltage reference value u_{gdref} u_{gqref} inside GSC controller	KVL	Internal application
[23]	Voltage	D-axis and Q-axis voltage reference value u_{gdref} u_{gqref} inside GSC controller	KVL	Internal application
[24]	Voltage	voltage reference value u_{ref} inside GSC controller	KVL	Internal application
[25]	Voltage	D-axis voltage reference value u_{gdref} inside GSC controller	KVL	Internal application
CSI-ECSC	Current	Current sampling loop outside GSC controller	KCL	External assembly

Table 3
Settled values of parameters of CSI-ECSC.

Parameters	Values	Parameters	Values
T_{c1}	1.0 s	$\alpha = T_{c2}/T_{c3}$	2.0
T_{c2}	0.04 s	$G_{c1} = 1/\alpha$	0.5
T_{c3}	0.02 s	K_c	1.0
T_{c4}	0.002 s		

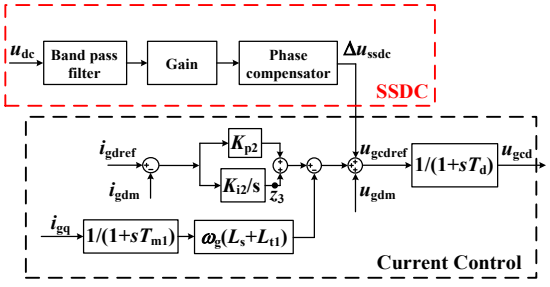

Fig. 9. SSDC scheme in the GSC controller.

order to enhance the sufficient supplementary control effect, K_c should not be too small. But, on the other hand, to prevent the system's balanced operating point from drifting too much, K_c should not be too big. And the ideal situation is that the additional control signals can produce slight changes in the amplitude and phase of sampled input current in GSC controller. Thus, the additional current signals' amplitudes are determined to be less than 10% of the original input current of the GSC controller. After calculation, the scope of K_c is decided to range from 1.0 to 10.0.

Fig. 8 (a), (b), and (c) show the root loci of the system with and without CSI-ECSC as the key parameters change. Under the conditions in Tables A1 and A2, several sets of eigenvalues graphs are drawn as T_{c3}, α, and K_c change, respectively. As shown in Fig. 8, under the condition of control variable, while T_{c3} decreases from 0.1 s to 0.01 s, α decreases

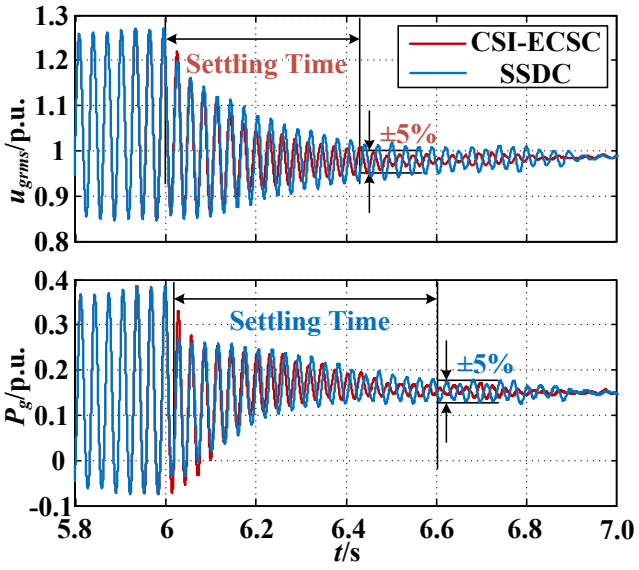

Fig. 10. Waveforms of u_{grms} and P_g at PCC of the system comparison between CSI-ECSC and SSDC.

from 10.0 to 2.0, K_c increases within the scope of 0.1 to 1.0, respectively, dominant poles move to the left. The effect of CSI-ECSC gets better and the stability margin becomes larger as K_c increases. All the three key parameters play an important role in the developed CSI-ECSC.

In PSCAD/EMTDC, the model of the target system with the CSI-ECSC shown in Figs. 4, 5 and 6 is built up. The simulation starts at 0 s and the oscillation takes place at 5.0 s. Four groups of parameters are shown in Table 1, where only one parameter changes at a time between two groups. According to the above theoretical analysis CSI-ECSC with different parameters on the system stability, the parameters are changed group by group in order to successively improve the stability of the system. The waveforms of u_{grms} and P_g at PCC in the system with four different groups of CSI-ECSC parameters are shown in Fig. 8 (d). At 6.0 s, CSI-ECSC is switched in. Comparing the simulation results from ***Group a*** to ***Group d***, we can find that: (1) CSI-ECSC can significantly damp the oscillations of voltage and power, as well as the system can be stabilized gradually to the original situation before oscillation occurs. (2) The decay speed of the oscillation amplitude gradually grows faster from ***Group a*** to ***Group d***, which indicates the time required for the system to stabilize turns shorter successively. (3) Likewise, the stable domain of the line length and the output power of WT are expanded by CSI-ECSC.

4.2. Comparison between CSI-ECSC and traditional SC

In this part, a contrast is made between the CSI-ECSC and other traditional SC works.

Firstly, Table 2 is drawn to compare several conventional SC works with the developed CSI-ECSC. Differences lie in the types of SC signals, SC signals coupling points, SC signals coupling types, and SC assembly mode.

Then, an effect comparison is conducted between the CSI-ECSC based on the parameters in Table 3 and another SC work. Fig. 9 presents a traditional supplementary control called supplementary subsynchronous damping control (SSDC) [25], which is composed of a band pass filter, a gain and a phase compensator. The band-pass filter is used to pick out the concerned signal and to avoid interference with the normal control function of GSC. The gain and the phase compensator can flexibly adjust the magnitude and phase of the signal to achieve better control performance. The SC signal Δu_{ssdc} is superposed into D-axis voltage reference signal u_{gcdref} based on Kirchoff's voltage law (KVL). Differences lie in the types of supplementary signals,

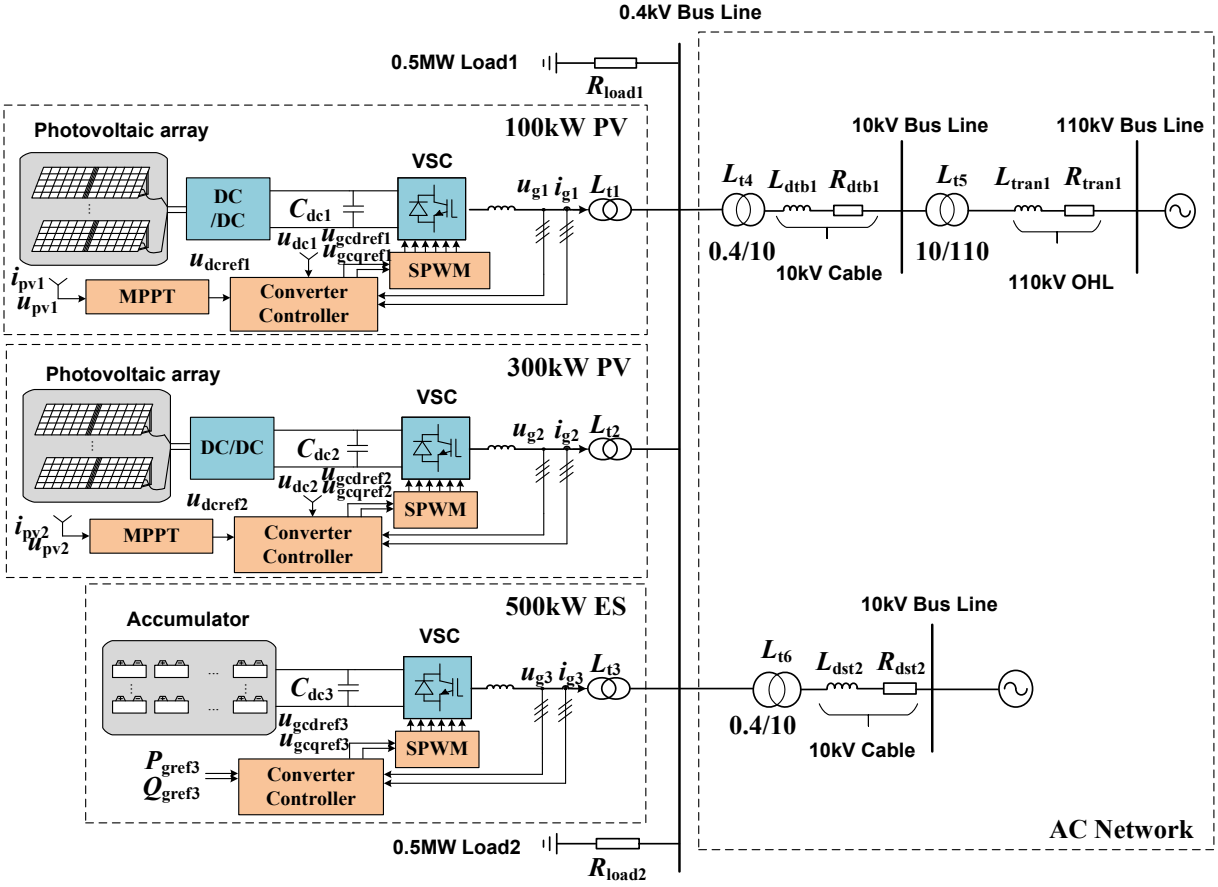

Fig. 11. Connection structure diagram of the ADN with PVs and ES.

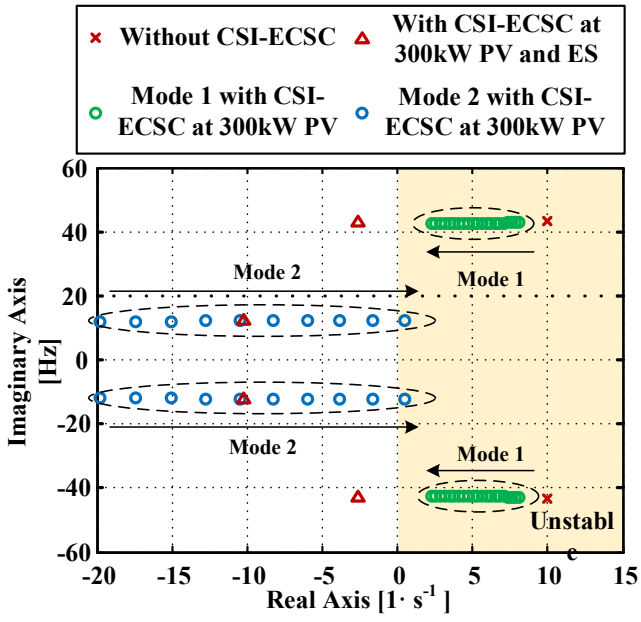

Fig. 12. Leading root loci of the ADN with PVs and ES.

supplementary signals coupling points, supplementary signals coupling types, and supplementary control assembly mode as shown in Table 3.

A simple effect comparison between the two SCs are discussed hereafter. The two types of control are both attached to the GSC controller of the target PMSG system. And the simulated waveforms of u_{grms} and P_g at PCC in the system under CSI-ECSC and SSDC are plotted in Fig. 10. After the two types of control are switched in at 6.0 s, the oscillations of voltage and power at PCC start to be damped rapidly. The settling time is defined to be the elapsed time before the output becomes bounded by two limits on either side of the steady-state output in [35,36]. Specified as ± 5%, the settling time of CSI-ECSC and SSDC is determined as 0.4 s and 0.6 s, respectively. The inhibition effect of CSI-ECSC is more rapid than that of SSDC. And 0.8 s after CSI-ECSC is switched in, the outputs turn to be steady-state and the oscillations of voltage and power begin to vanish, while it takes 1.0 s for SSDC to accomplish that. Therefore, the developed CSI-ECSC can not only achieve equal effects as the traditional supplementary control does, but also can be assembled more conveniently without changing the inner physical structure of GSC controller.

4.3. Effect verification in ADN with PV and ES

In this part the proposed CSI-ECSC is applied to a more complex ADN with photovoltaics (PVs) and energy storage (ES). Similarly, eigenvalue analysis and simulation verification are conducted.

Fig. 11 shows the diagram of the ADN with PVs and ES. In this ADN, there are an 100 kW PV, a 300 kW PV, and a 500 kW ES connected at the same PCC at 0.4 kV bus line. Considering ES is usually equipped to absorb the power fluctuation, the CSI-ECSC is applied at ES to enhance the capability of the ADN to accept local intermittent power fluctuation. And the CSI-ECSC at 300 kW PV is applied to optimize dynamic characteristic of PV under more serious power randomness and uncertainty of larger capacity [37].

Following the same process in previous system, the small signal mathematical model of the ADN with PVs and ES is set up firstly. After eigenvalues are calculated, two leading root loci of the ADN with PVs

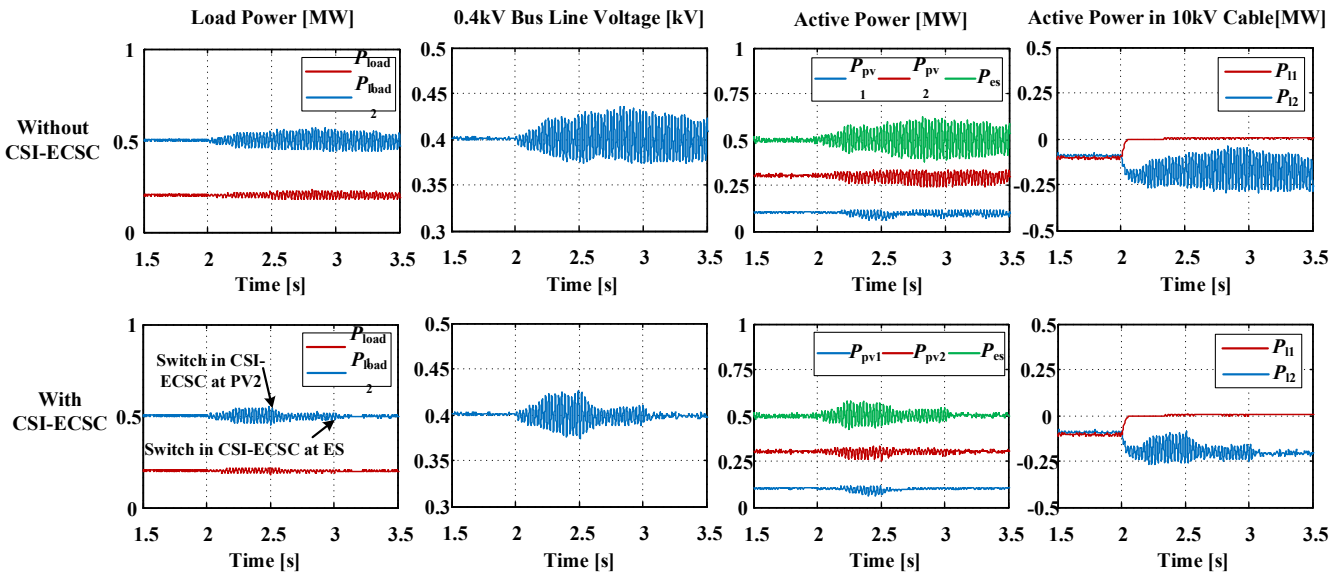

Fig. 13. Waveforms of load power, 0.4 kV bus line voltage, active power of each units, and active power in 10 kV cable are drawn with and without CSI-ECSC in simulation.

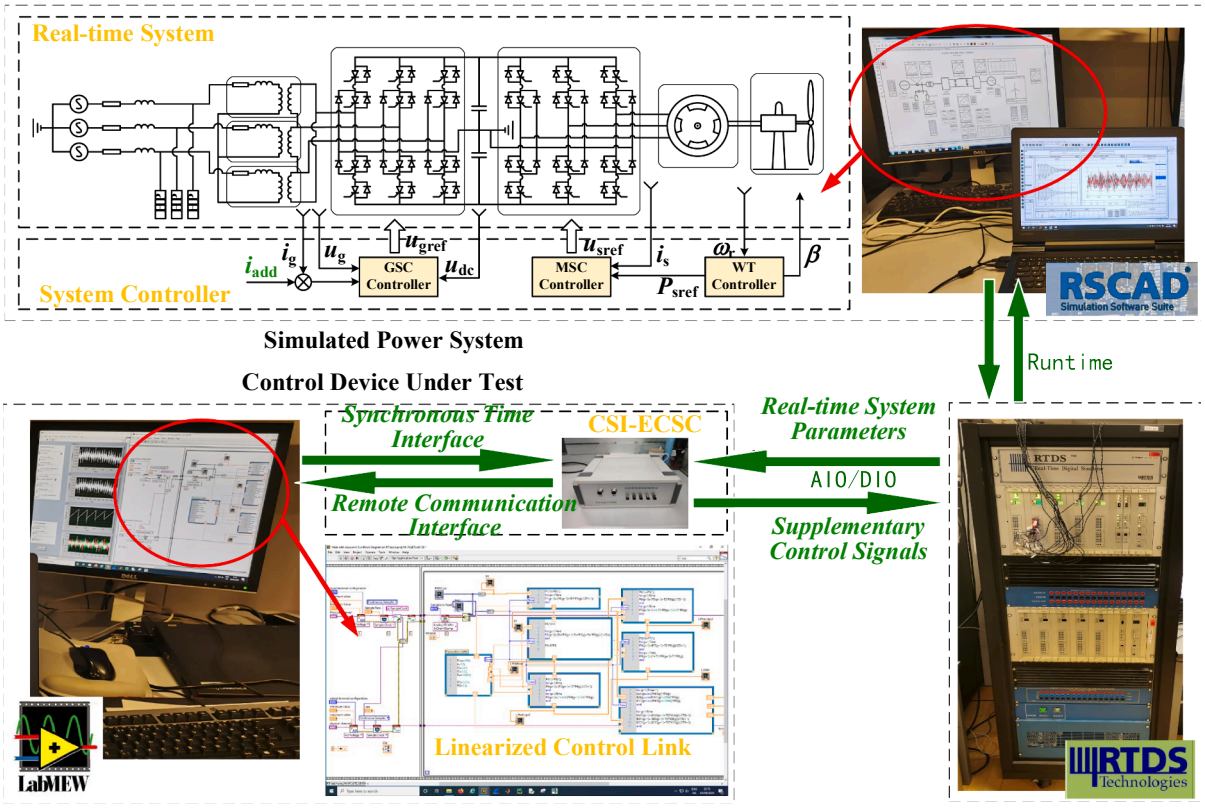

Fig. 14. The general structure of HIL testing on developed CSI-ECSC and physical picture of the HIP testing platform.

and ES are plotted in Fig. 12. Red "x" represents eigenvalues of the system without CSI-ECSC, and the related system is unstable. Green "o" represents Mode 1 root locus of the system with CSI-ECSC at 300 kW PV as gain K_c changes from −1.0 to −3.0, blue "o" represents Mode 2 root locus. It can be seen that before the Mode 1 root locus extends to the left half plane, the mode 2 root locus has already extended to the right half plane. In this case, only assembling CSI-ECSC at 300 kW PV cannot improve stability of the system effectively. Hereby, ES is also equipped with CSI-ECSC, and the eigenvalues are represented by red "Δ" in Fig. 12. When 300 kW PV and ES are configured with CSI-ECSC, both

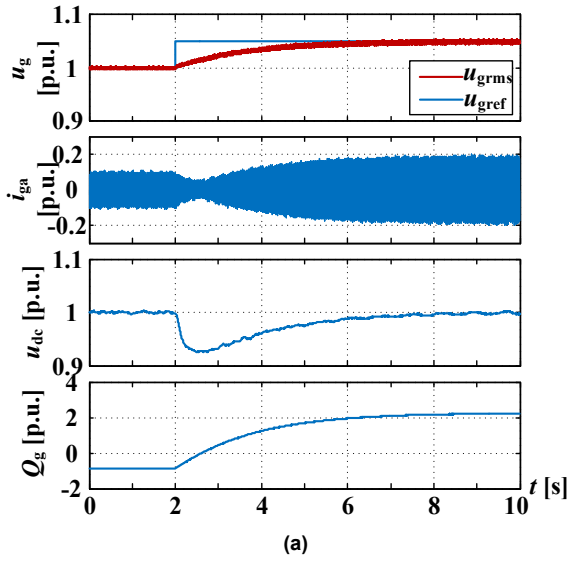

Fig. 15. Waveforms of current ($I_{AP}/I_{BP}/I_{CP}$), voltage (V_{ACPCC}/V_{DC}), and power (P_{NPCC}/Q_{NPCC}) at PCC under changes of (a) AC voltage reference value, (b) wind speed.

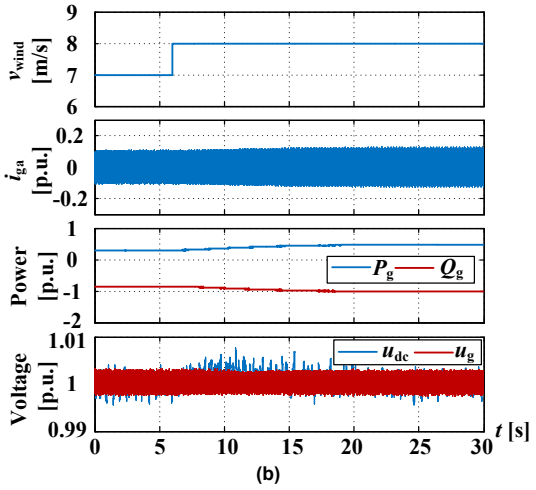

Fig. 16. Generation process of supplementary current signals in CSI-ECSC.

Table 4
Parameters of supplementary control for simulation verification.

Paras	T_{c1}[s]	T_{c2}[s]	T_{c3}[s]	T_{c4}[s]	K_c
Case 1	0.1	0.5	0.02	0.002	4.0
Case 2	1.0	0.47	0.02	0.5	7.0
Case 3	1.0	0.5	0.02	0.5	4.0

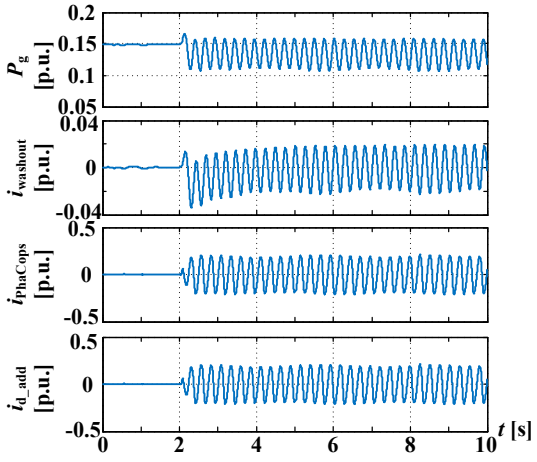

Fig. 17. Comparison of three cases of waveforms of AC/DC voltage and active/reactive power at PCC in RT HIL test of CSI-ECSC.

Mode 1 and Mode 2 eigenvalues move to the left half of the plane, which means the system turns stable.

In PSCAD/EMTDC, the ADN with PVs and ES is established to validate the effectiveness of CSI-ECSC in the system. In Fig. 13, the waveforms of load power, 0.4 kV bus line voltage, active power of each units, and active power in 10 kV cable are drawn with and without CSI-ECSC, respectively. Due to the disturbance caused by the switching of operating modes at 2.0 s, an oscillation with frequency 43 Hz occurs. At 2.5 s, the CSI-ECSC is switched in at 300 kW PV. The divergence trend of the system oscillation can be retrained. But the oscillation still maintains an obvious constant amplitude. At 3.0 s, the CSI-ECSC is switched in at ES, the oscillation is obviously suppressed and the system becomes stable again.

5. Real-time hardware in the loop test of CSI-ECSC based on RTDS

This section conducts a real-time hardware-in-the-loop test of CSI-ECSC based on real-time digital simulation to verify the actual control effect of physical controller.

5.1. Real-time HIP testing implementation

The HIL testing is recognized as an effective approach to do verification testing, and it is widely used to conduct laboratory experiments of the new developed system [38–40]. Due to time delays and noise in the hardware loop, the control effects of designed controllers might differ from the situations in theory and simulation. Fig. 14 shows the general structure of the HIL testing on developed CSI-ECSC and the physical picture of the HIP testing platform. In the HIL testing platform, hardware devices are interfaced to a real-time simulator (RTS), which models the rest of the system, and they are used to test the devices' operations. We choose Real-Time Digital Simulator (RTDS) to develop this HIL platform. In RSCAD (a graphical user interface where the user is able to construct, run and analyze simulation cases), the model of a D-PMSG grid-connected system by distribution line with its controller is set up. To achieve the function of fast and reliable measurement, a detailed model of CSI-ECSC is developed in the Laboratory Virtual Instrument Engineering Workbench (LabVIEW) real-time environments in another

hardware device. As shown in Fig. 14, each control link of CSI-ECSC is linearized and the output of each link is monitored by oscilloscopes in LabVIEW.

In this way, the conducted control hard-in-the-loop (CHIL) simulations are closed-loop ones in structure, where real-time system parameters (θ_{PLL}, u_g, i_g) are sent from the RTDS to the CSI-ECSC and the response of the CSI-ECSC (i_{a_add}, i_{b_add}, i_{c_add}) is fed back to the RTDS.

5.2. Case study and experimental results

In this part, the experimental results of the HIL testing will be presented, including control response of the target system in Scenario-1, generation process of supplementary current signals in CSI-ECSC in Scenario-2, and effect verification of CSI-ECSC in Scenario-3.

1) Scenario-1: Control response of the target system

In RSCAD, based on the target system model with its control system, this case studies the control response for verifying the feasibility of target system under the changed operational conditions. Fig. 15 shows the waveforms of current i_{ga}, voltage u_g, and power P_g and Q_g at PCC when AC voltage reference u_{gref} value and wind speed v_{wind} change. When the system is in a stable state, and when u_{gref} is switched from 1.0 [p.u.] to 1.05 [p.u.] at 2.0 s, transition to a new stable state takes 6 s. Amplitude of current increases from 0.1kA to 0.2kA, AC voltage increases up to 1.05 [p.u.] under control. DC voltage falls down to 0.93 [p.u.] and gradually returns to the reference value of 1.0 [p.u.]. Similarly, when wind speed changes from 7 m/s to 8 m/s, the system tends to be stable again after experiencing a dynamic fluctuation process. The built-up real-time system works well under the current operating conditions.

2) Scenario-2: Generation process of supplementary current signals in CSI-ECSC

The CSI-ECSC monitors active power at PCC through the real-time and synchronous sampling of instantaneous

voltage and current. As shown in Fig. 16, after the washout link, the DC component of the sampled signal is filtered out, the signal in the loop is defined as $i_{washout}$. Via phase compensator links, $i_{washout}$ is transferred to $i_{PhaCops}$ by adjusting the phase of the signal in the loop. It can be seen that i_{dref} contains the state information of active power fluctuation and stays at zero before oscillation is provoked.

3) Scenario-3: Effect verification of CSI-ECSC

In this scenario, the control effect of CSI-ECSC is verified based on real-time HIL testing. In three cases, three groups of CSI-ECSC control parameters are implemented as shown in Table 4, in order to compare the control effects in different parameter settings. When CSI-ECSC is switched in at 2.0 s by superposing ($i_{a\_add}/i_{b\_add}/i_{c\_add}$) on $i_a/i_b/i_c$, the waveforms of typical electric quantities are shown in Fig. 17. It can be seen that the effects of CSI-ECSC in different cases vary in fluctuations suppression degrees. In Case 1, oscillations are not damped completely (greater than ± 5% of rating level) after CSI-ECSC is switched in and begin to repeat at 5.0 s. In Case 2, oscillation amplitude is suppressed to a certain extent. In Case 3, the control effect of CSI-ECSC is the best as the amplitude of oscillation is damped to ± 5% of rating level in 2 s, and to ±2% of rating level in 4 s. For this case, a good effect of CSI-ECSC can be obtained. On the one hand, comparison among the three cases, the experimental results of RT HIL test verify that under the set-up platform the developed CSI-ECSC could effectively suppress oscillation of voltage and power at PCC. On the other hand, it can be concluded from different quantities' waveforms that the damping effects of DC voltage and active power are better than those of AC voltage and reactive power. The reason is that the CSI-ECSC focuses on the active power fluctuation of GSC. And the coupling point of the SC signals are closely related with DC voltage control in GSC.

Therefore, the CSI-ECSC has been proved to be useful to damp oscillations at PCC, where converters are applied to connect the unit with power system. With parameters optimization, we can greatly improve the effects of the CSI-ECSC to make it suitable with multiple working conditions. Also, to explore the potential functions with different working mode, we can adjust the inputting type of signals in the future.

6. Conclusion

A novel supplementary control method called CSI-ECSC is proposed to improve the dynamic characteristics of ADNs. Specifically, coupling SC signals to current sampling loop makes it no longer necessary to redesign the internal physical structure of the existing controller. Hence, the assembling and workability of SC is improved and simplified. Theoretical analysis and experimental results of the proposed CSI-ECSC provide a new thought and scheme of SC application. To the problem of low efficiency, and high-cost assembling and management of SC in power system, this paper proposes a potential solution. The main achievements of this paper are as follows:

1) Based on full eigenvalues and sets of simulations in PSCAD/EMTDC, the CSI-ECSC is proved to be effective to damp oscillations in an ADN with PMSG. Both parameter setting and optimization process confirm that the settle time of voltage and power can be reduced to 0.4 s as the system keeps unattenuated oscillations.
2) The CSI-ECSC improves dynamic characteristics of ADNs with multiple converter-based DGs and active loads. Its damping effect is validated as good as that of traditional SCs (such as SSDC). Also, its applicability is evaluated further by applying the CSI-ECSC in a more complex AND with PVs and ESs.
3) Under the HIL test based on RTDS, the proposed CSI-ECSC has been successfully implemented. Considering time delays and noise in the hardware loop, the performance is optimized by adjusting parameters. Experimental results produce evidence about the effects. Moreover, this paper puts forward a potential solution to the problem of low efficiency, high-cost assembling and management on SC's application in power system.

The future works will be focused on the optimization of the developed CSI-ECSC. More than one mode of operation can be designed by switching inputting types of signal, such as DC voltage (active power) mode and AC voltage (reactive power) mode. Furthermore, large-scale coordinated control of the CSI-ECSC in ADNs shall be investigated where multi units of CSI-ECSCs are used together to improve stability of the system. Also, a field test is to be undertaken to verify its effects and reliability.

Declaration of Competing Interest

The authors declare that they have no known competing financial interests or personal relationships that could have appeared to influence the work reported in this paper.

Acknowledgments

This work was supported by the National Key Research and Development Program of China under Grant 2017YFB0902800.

Appendix A

Parameters of target system.
(See Tables A1 and A2).

Table A1
Electrical parameters of target system.

Parameters	Description	Values [unit]
C_{dc}	DC capacitance between GSC and MSC	0.03 [F]
u_{dc}	Instantaneous value of DC voltage of MSC and GSC	1.5 [kV]
ω_b	Reference value of system angular velocity	100π |rad/s]
P_s	Instantaneous value of DC output active power of GSC	0.3 [MW]
L_s	Port filter inductance of GSC	0.182 [mH]
L_{t1}	Leakage inductance of grid-connected 0.69/10 transformer	0.3 [p.u.]
R_f	Resistance of high-pass filter	227 [Ω|
L_f	Inductance of high-pass filter	0.038 [H]
C_f	Capacitance of high-pass filter	0.73 [μF]
R_{Dist_Line}	Resistance of distribution line	13.2 [Ω| (40 km)
L_{Dist_Line}	Inductance of distribution line	0.0436[H] (40 km)
L_{t2}	Leakage inductance of 10/110 transformer T_2	0.1 [p.u.]
R_{Trans_Line}	Resistance of transmission line	4 [Ω||(50 km)
L_{Trans_Line}	Inductance of transmission line	0.0595[H] (50 km)

Appendix B

State space equations of target system.
AC systems.

Table A2
Control parameters of target system.

Parameters	Description	Values [unit]
T_{m1}	Filter time constant of instantaneous value of current and voltage at PCC	0.002 [s]
T_{m2}	Filter time constant of effective value of voltage and power at PCC	0.02 [s]
T_s	Switching time constant of GSC	1/2000 [s]
T_d	Switching time constant of modulation	$1.5T_s$
u_{dcref}	Reference value of DC voltage	1.0 [p.u.]
u_{gref}	Reference value of AC voltage at PCC	1.0 [p.u.]
K_{p1}	Proportional gain of DC voltage control	1.0 [p.u.]
K_{p2}	Proportional gain of current control	0.73 [p.u.]
K_{p3}	Proportional gain of AC voltage control	1.0 [p.u.]
K_{p4}	Proportional gain of current control	0.73 [p.u.]
K_{p5}	Proportional gain of PLL	50.0 [p.u.]
K_{i1}	Integral gain of DC voltage control	1/0.2 [p.u./s]
K_{i2}	Integral gain of inner loop current control	1/0.03 [p.u./s]
K_{i3}	Integral gain of AC voltage control	1/0.2 [p.u./s]
K_{i4}	Integral gain of inner loop current control	1/0.03 [p.u./s]
K_{i5}	Integral gain of PLL	1/0.004[p.u./s]

$$\frac{\mathrm{d}}{\omega_b \mathrm{d}t}\begin{bmatrix} i_{gd} \\ i_{gq} \end{bmatrix} = \frac{1}{L_{t1}+L_s}\begin{bmatrix} u_{gd}-u_{gcd} \\ u_{gq}-u_{gcq} \end{bmatrix} + \begin{bmatrix} 0 & \omega_g \\ -\omega_g & 0 \end{bmatrix}\begin{bmatrix} i_{gd} \\ i_{gq} \end{bmatrix} \tag{15}$$

$$\frac{\mathrm{d}}{\omega_b \mathrm{d}t}\begin{bmatrix} i_{ld} \\ i_{lq} \end{bmatrix} = \frac{1}{L_l}\begin{bmatrix} u_{gd}-E_d \\ u_{gq}-E_q \end{bmatrix} + \begin{bmatrix} -\dfrac{R_l}{L_l} & \omega_g \\ -\omega_g & -\dfrac{R_l}{L_l} \end{bmatrix}\begin{bmatrix} i_{ld} \\ i_{lq} \end{bmatrix} \tag{16}$$

$$u_g^2 = u_{gd}^2 + u_{gq}^2 \tag{17}$$

$$\begin{cases} R_l = R_{Dist\backslash\_Line} + R_{Trans\backslash\_Line} \\ L_l = L_{Dist\backslash\_Line} + L_{T2} + L_{Trans\backslash\_Line} \end{cases} \tag{18}$$

$$\frac{\mathrm{d}}{\omega_{\mathrm{b}}\mathrm{d}t}\begin{bmatrix} i_{\mathrm{fd}} \\ i_{\mathrm{fq}} \end{bmatrix} = \frac{1}{L_{\mathrm{f}}}\begin{bmatrix} u_{\mathrm{gd}} - u_{\mathrm{fd}} \\ u_{\mathrm{gq}} - u_{\mathrm{fq}} \end{bmatrix} + \begin{bmatrix} 0 & \omega_{\mathrm{g}} \\ -\omega_{\mathrm{g}} & 0 \end{bmatrix}\begin{bmatrix} i_{\mathrm{fd}} \\ i_{\mathrm{fq}} \end{bmatrix} \tag{19}$$

$$\frac{\mathrm{d}}{\omega_{\mathrm{b}}\mathrm{d}t}\begin{bmatrix} u_{\mathrm{fd}} \\ u_{\mathrm{fq}} \end{bmatrix} = -\frac{1}{C_{\mathrm{f}}}\begin{bmatrix} i_{\mathrm{ld}} + i_{\mathrm{gd}} \\ i_{\mathrm{lq}} + i_{\mathrm{gq}} \end{bmatrix} + \begin{bmatrix} 0 & \omega_{\mathrm{g}} \\ -\omega_{\mathrm{g}} & 0 \end{bmatrix}\begin{bmatrix} u_{\mathrm{fd}} \\ u_{\mathrm{fq}} \end{bmatrix} \tag{20}$$

$$R_{\mathrm{f}}\left(\begin{bmatrix} i_{\mathrm{fd}} \\ i_{\mathrm{fq}} \end{bmatrix} + \begin{bmatrix} i_{\mathrm{ld}} \\ i_{\mathrm{lq}} \end{bmatrix} + \begin{bmatrix} i_{\mathrm{gd}} \\ i_{\mathrm{gq}} \end{bmatrix}\right) + \begin{bmatrix} u_{\mathrm{gd}} \\ u_{\mathrm{gq}} \end{bmatrix} - \begin{bmatrix} u_{\mathrm{fd}} \\ u_{\mathrm{fq}} \end{bmatrix} = 0 \tag{21}$$

DC capacitor.

$$C_{\mathrm{dc}}u_{\mathrm{dc}}\frac{\mathrm{d}u_{\mathrm{dc}}}{\omega_{\mathrm{b}}\mathrm{d}t} = P_{\mathrm{s}} + u_{gcd}i_{\mathrm{gd}} + u_{\mathrm{gcq}}i_{\mathrm{gq}} \tag{22}$$

Control system of GSC.

$$T_{\mathrm{m1}}\frac{\mathrm{d}}{\mathrm{d}t}\begin{bmatrix} i_{\mathrm{gdm}} \\ i_{\mathrm{gqm}} \\ u_{\mathrm{gdm}} \\ u_{\mathrm{gqm}} \end{bmatrix} + \begin{bmatrix} i_{\mathrm{gdm}} \\ i_{\mathrm{gqm}} \\ u_{\mathrm{gdm}} \\ u_{\mathrm{gqm}} \end{bmatrix} = \begin{bmatrix} i_{\mathrm{gd}} \\ i_{\mathrm{gq}} \\ u_{\mathrm{gd}} \\ u_{\mathrm{gq}} \end{bmatrix} \tag{23}$$

$$T_{\mathrm{m2}}\frac{\mathrm{d}}{\mathrm{d}t}u_{\mathrm{gm}} + u_{\mathrm{gm}} = u_{\mathrm{g}} \tag{24}$$

$$\begin{cases} \dot{z}_1 = u_{\mathrm{dcref}} - u_{\mathrm{dc}} \\ \dot{z}_2 = u_{\mathrm{gref}} - u_{\mathrm{gm}} \\ \dot{z}_3 = K_{\mathrm{p1}}(u_{\mathrm{dcref}} - u_{\mathrm{dc}}) + K_{\mathrm{i1}}z_1 - i_{\mathrm{gdm}} \\ \dot{z}_4 = K_{\mathrm{p3}}(u_{\mathrm{gref}} - u_{\mathrm{gm}}) + K_{\mathrm{i3}}z_2 - i_{\mathrm{gqm}} \end{cases} \tag{25}$$

$$\begin{cases} -\left[K_{\mathrm{p1}}(u_{\mathrm{dcref}} - u_{\mathrm{dc}}) + K_{\mathrm{i1}}z_1 - i_{\mathrm{gdm}}\right]K_{\mathrm{p2}} - \\ K_{\mathrm{i2}}z_3 + \omega_{\mathrm{g}}(L_{\mathrm{t1}} + L_{\mathrm{s}})i_{\mathrm{gqm}} + u_{\mathrm{gdm}} - u_{\mathrm{gcdref}} = 0 \\ -\left[K_{\mathrm{p3}}(u_{\mathrm{gref}} - u_{\mathrm{gm}}) + K_{\mathrm{i3}}z_2 - i_{\mathrm{gqm}}\right]K_{\mathrm{p4}} - \\ K_{\mathrm{i4}}z_4 - \omega_{\mathrm{g}}(L_{\mathrm{t1}} + L_{\mathrm{s}})i_{\mathrm{gdm}} + u_{\mathrm{gqm}} - u_{\mathrm{gcqref}} = 0 \end{cases} \tag{26}$$

PLL.

$$\begin{cases} \dfrac{\mathrm{d}}{\mathrm{d}t}z_5 = u_{\mathrm{gq}} \\ \dfrac{\mathrm{d}}{\mathrm{d}t}\theta_{\mathrm{PLL}} = K_{\mathrm{p5}}u_{\mathrm{gq}} + K_{\mathrm{i5}}z_5 + \omega_0 \end{cases} \tag{27}$$

$$\omega_{\mathrm{b}}\omega_{\mathrm{g}} - K_{\mathrm{p5}}u_{\mathrm{gq}} - K_{\mathrm{i5}}z_5 - \omega_0 = 0 \tag{28}$$

Converter switching and modulation.

$$\frac{\mathrm{d}}{\mathrm{d}t}\begin{bmatrix} u_{\mathrm{gcd}} \\ u_{\mathrm{gcq}} \end{bmatrix} = \frac{1}{T_{\mathrm{d}}}\begin{bmatrix} u_{\mathrm{gcdref}} \\ u_{\mathrm{gcqref}} \end{bmatrix} - \frac{1}{T_{\mathrm{d}}}\begin{bmatrix} u_{\mathrm{gcd}} \\ u_{\mathrm{gcq}} \end{bmatrix} \tag{29}$$

Coordinate transformation.

$$\delta = \theta_{\mathrm{PLL}} - (\omega_0 t + \delta_0) \tag{30}$$

$$\begin{bmatrix} E_{\mathrm{d}} \\ E_{\mathrm{q}} \end{bmatrix} - E\begin{bmatrix} cos\delta \\ -sin\delta \end{bmatrix} = 0 \tag{31}$$

References

[1] Shafiu A, Bopp T, Chilvers I, Strbac G, Jenkins N, Li HY. Active management and protection of distribution networks with distributed generation. 2004 IEEE power engineering society general meeting. IEEE; 2004. p. 1–6.

[2] Jia YY, Yang LX, Wang Z. Impact of the active management and active control on the survivability of distribution network structure. 2015 5th international conference on electric utility deregulation and restructuring and power technologies. IEEE; 2015. p. 1251–5.

[3] Georgilakis PS, Hatziargyriou ND. Optimal distributed generation placement in power distribution networks: models, methods, and future research. IEEE Trans Power Systems 2013;28(3):3420–8.

[4] Mohiuddin SM, Mahmud MA, Haruni AMO, Pota HR. Design and implementation of partial feedback linearizing controller for grid-connected fuel cell systems. Int J Electr Power Energy Syst 2017;93:414–25.

[5] Nguyen DT, Nguyen HT, Le LB. Dynamic pricing design for demand response integration in power distribution networks. IEEE Trans Power Systems 2016;31(5):3457–72.

[6] Roy NK, Pota HR, Mahmud MA, Hossain MJ. Key factors affecting voltage oscillations of distribution networks with distributed generation and induction motor loads. Int J Electr Power Energy Syst 2013;53:515–28.

[7] Hung DQ, Mithulananthan N. Multiple distributed generator placement in primary distribution networks for loss reduction. IEEE Trans Ind Electron 2013;60(4):1700–8.

[8] Enslin JHR, Heskes PJM. Harmonic interaction between a large number of distributed power inverters and the distribution network. IEEE Trans Power Electron 2004;19(6):1586–93.

[9] Zhao XF, Qiu YD, Li Q, Yang X, Tang MJ, Wen B. Simulation analysis and suppression method of PT low frequency oscillation in distribution network. In: IEEE international conference on power system technology. IEEE; 2018. p. 3151–7.

[10] Gill S, Kockar I, Ault GW. Dynamic optimal power flow for active distribution networks. IEEE Trans Power Syst 2014;29(1):121–31.

[11] Zhu XR, Zhang JC, Wang Y. supplementary control of DFIG for inter-area oscillation damping. In: IECON 2014-40th annual conference of the IEEE industrial electronics society. IEEE; 2015. p. 5599–605.

[12] Guo WT, Liu F, Si J, Mei SW. Online and model-free supplementary learning control based on approximate dynamic programming. 2014 The 26th Chinese Control and Decision Conference. IEEE; 2014. p. 1316–21.
[13] Lee Y, Yoo E, Lee T, Moon UC. Supplementary control of conventional coordinated control for 1000 MW ultra-supercritical thermal power plant using dynamic matrix control. J Electr Eng Technol 2018;13(1):97–104.
[14] Mithulananthan N, Canizares CA, Reeve J, Rogers GJ. Comparison of PSS, SVC, and STATCOM controllers for damping power system oscillations. IEEE Trans Power Syst 2003;18(2):786–92.
[15] Cai LJ, Erlich I. Simultaneous coordinated tuning of PSS and FACTS damping controllers in large power systems. IEEE Trans Power Syst 2005;20(1):294–300.
[16] Ginarsa IM, Soeprijanto A, Purnomo MH. Controlling chaos and voltage collapse using an ANFIS-based composite controller-static var compensator in power systems. Int J Electr Power Energy Syst 2013;46:79–88.
[17] Li S, Xu L, Haskew TA. Control of VSC-based STATCOM using conventional and direct-current vector control strategies. Int J Electr Power Energy Syst 2013;45(1):175–86.
[18] Morris D. Linear control systems engineering. McGraw-Hill Higher Education; 1995.
[19] Delghavi MB, Yazdani A. An adaptive feedforward compensation for stability enhancement in droop-controlled inverter-based microgrids. IEEE Trans Power Delivery 2011;26(3):1764–73.
[20] Karimi H, Davison EJ, Iravani R. Multivariable servomechanism controller for autonomous operation of a distributed generation unit: design and performance evaluation. IEEE Trans Power Syst 2010;25(2):853–65.
[21] Balasubramanyam PV, Parameswaran S, Murthy PRM. Analysis and Damping of Torsional Oscillations Through Supplementary Excitation Control. TENCON '91. Region 10 International Conference on EC3-Energy, Computer, Communication and Control Systems. IEEE; 1991. p. 1–10.
[22] Majumder R, Chaudhuri B, Ghosh A, Majumder R, Ledwich G, Zare F. Improvement of stability and load sharing in an autonomous microgrid using supplementary droop control loop. IEEE Trans Power Syst 2010;25(2):796–808.
[23] Haddadi A, Yazdani A, Joos G, Boulet B. A gain-scheduled decoupling control strategy for enhanced transient performance and stability of an islanded active distribution network. IEEE Trans Power Delivery 2014;29(2):560–9.
[24] Guerrero JM, GarciadeVicuna L, Matas J, Castilla M, Miret J. A wireless controller to enhance dynamic performance of parallel inverters in distributed generation systems. IEEE Trans Power Electron 2004;19(5):1205–13.
[25] Liu H, Xie X, He J, Xu T, Yu Z, Wang C, et al. Subsynchronous interaction between direct-drive PMSG based wind farms and weak AC networks. IEEE Trans Power Syst 2017;32(6):4708–20.
[26] Sambariya DK, Prasad R. Robust tuning of power system stabilizer for small signal stability enhancement using metaheuristic bat algorithm. Int J Electr Power Energy Syst 2014;61:229–38.
[27] Tan J, Wang XR, Chen Z, Li M. Impact of a direct-drive permanent magnet generator (DDPMG) wind turbine system on power system oscillations. 2012 IEEE Power and Energy Society General Meeting. IEEE; 2012. p. 1–8.
[28] Sun J. Small-signal methods for ac distributed power systems-a review. IEEE Trans Power Electron 2009;24(11):2545–54.
[29] Prommee P, Thongdit P, Angkeaw K. Log-domain high-order low-pass and band-pass filters. AEU-Int J Electron Commun 2017;79:234–42.
[30] Ghaffari A, Klumperink EAM, Soer MCM, Nauta B. Tunable High-Q N-Path Band-Pass Filters: Modeling and Verification. IEEE J Solid-State Circuits 2011;46(5):998–1010.
[31] Coelho EAA, Cortizo PC, Garcia PFD. Small-signal stability for parallel-connected inverters in stand-alone AC supply systems. IEEE Trans Ind Appl 2002;38(2):533–42.
[32] Mondal D, Chakrabarti A, Sengupta A. Optimal placement and parameter setting of SVC and TCSC using PSO to mitigate small signal stability problem. Int J Electr Power Energy Syst 2012;42(1):334–40.
[33] Tan J, Wu WH, Wang XR, Chen Z. Effect of tower shadow and wind shear in a wind farm on AC tie-line power oscillations of interconnected power systems. Energies 2013;6(12):6352–72.
[34] Huang B, Sun H, Liu Y, Wang L, Chen Y. Study on subsynchronous oscillation in D-PMSGs-based wind farm integrated to power system. IET Renew Power Gener 2019;13(1):16–26.
[35] Mohamed Imran A, Kowsalya M, Kothari DP. A novel integration technique for optimal network reconfiguration and distributed generation placement in power distribution networks. Int J Electr Power Energy Syst 2014;63:461–72.
[36] Moravej Z, Akhlaghi A. A novel approach based on cuckoo search for DG allocation in distribution network. Int J Electr Power Energy Syst 2013;44(1):672–9.
[37] Yazdani A, Dash pp. A control methodology and characterization of dynamics for a photovoltaic (PV) system interfaced with a distribution network. IEEE Trans Power Delivery 2009;24(3):1538–51.
[38] Ali P, Hamid RB, Mohamad EI, Gevork BG, Guerrero JM. Real-time simulator and offline/online closed-loop test bed for power system modeling and development. Int J Electr Power Energy Syst 2020;122:1–16.
[39] Kotsampopoulos P, Lagos D, Hatziargyriou N, Faruque MO, Lauss G, Nzimako O, et al. A benchmark system for hardware-in-the-loop testing of distributed energy resources. IEEE Power Energy Technol Syst J 2018;5(3):94–103.
[40] Muhamad TA, Sofizan NY, Sheikh A, Mohd S, Nira S, Nur A. Real-time hardware-in-the-loop testing platform for wide area protection system in large-scale power systems. 2019 IEEE International Conference on Automatic Control and Intelligent Systems. IEEE; 2019. p. 210–5.